Role of polyol in the synthesis of Fe particles

R. Justin Joseyphus[a], D. Kodama[a], T. Matsumoto[b], Y. Sato[a], B. Jeyadevan[a,*], K. Tohji[a]

[a]Graduate School of Environmental Studies, Tohoku University, Aramaki, Aoba-ku, Sendai, Miyagi 980-8579, Japan
[b]Division of Materials Control, Institute of Multidisciplinary Research for Advanced Materials, Tohoku University, Sendai 980-8577, Japan

Available online 30 November 2006

Abstract

Though there have been reports on the synthesis of Fe particles by using polyol process, the role of polyol has not been understood well and it still remains unclear. We report the successful synthesis of Fe nanoparticles in liquid polyols, their magnetic properties and also the influence of polyols for the formation of Fe nanoparticles. The oxide phase fraction and the magnetic properties are found to depend on the particle size of the Fe synthesized in various polyols like trimethylene glycol, propylene glycol and ethylene glycol.
© 2006 Elsevier B.V. All rights reserved.

PACS: 75.50.Bb; 75.50.Tt; 74.25.Ha

Keywords: Polyol process; Fe nanoparticle

1. Introduction

Among various chemical techniques available for the synthesis of metallic and alloy nanoparticles, polyol process stands out since the polyol medium prevents the particle from coming into contact with the oxidizing atmosphere. Though most of the transition metals were reduced successfully by polyol, the formation of iron in polyol is claimed only through disproportionation reaction of ferrous salts [1]. However, the formation of alloys such as FePt [2], FePd, FeCo, etc. were reported recently and cast a doubt on the disability of the polyol in reducing iron. Therefore, in this paper, we attempted the synthesis of Fe nanoparticles using polyol process and elucidate the role of polyol. The magnetic properties of the particles are also reported.

2. Experimental

The precursors used for the synthesis of Fe nanoparticles are $FeCl_2 \cdot 4H_2O$ and NaOH. The synthesis was attempted using polyols like trimethylene glycol (TMEG), propylene glycol (PG) and ethylene glycol (EG). The precursors were taken in a reaction vessel containing 100 ml of polyol and heated to the desired temperature with constant mechanical stirring. The synthesized samples were washed and stored in alcohol. The structure, morphology and magnetic properties of the particles were analyzed by X-ray diffraction (XRD) using a Cu target, scanning electron microscope (SEM) and vibration sample magnetometer (VSM).

3. Results and discussion

3.1. Synthesis of Fe in various polyols

The synthesis of Fe in polyols was attempted by reducing ferrous ions ($FeCl_2 \cdot 4H_2O$) in the presence of hydroxyl ion. The formation of the iron particles as a function of (a) type of polyol, (b) ferrous salts, (c) ferrous ion concentration, (d) hydroxyl ion concentration and (e) reaction temperature were studied in detail. However, this report will discuss the results pertaining to the Fe molar concentration of 0.02 M, OH/Fe ratio of 10 and reaction temperature of 393 K in different types of polyol. Fig. 1 shows the XRD pattern of the products synthesized in TMEG, PG and EG. Average grain sizes of the Fe nanoparticles synthesized in TMEG, PG and EG are 15, 23 and 32 nm, respectively, determined using Scherrer's formula. Depending on the

*Corresponding author. Tel.: 81 22 795 7412; fax: 81 22 795 7412.
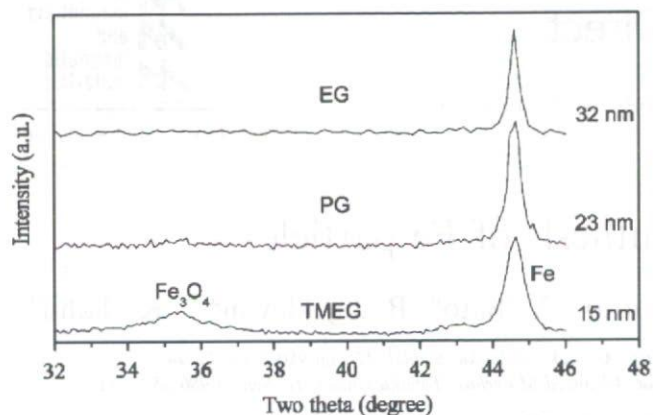E-mail address: jeya@mail.kankyo.tohoku.ac.jp (B. Jeyadevan).

Fig. 1. XRD pattern of the Fe nanoparticles synthesized in various polyols.
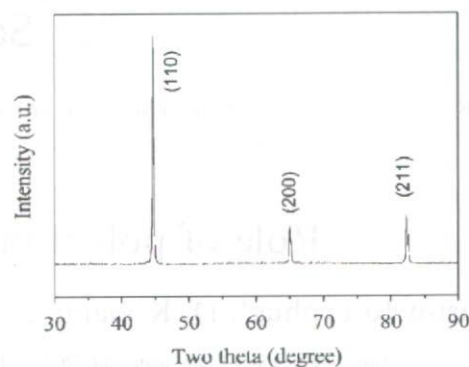

Fig. 2. XRD pattern of the Fe particles synthesized in EG.
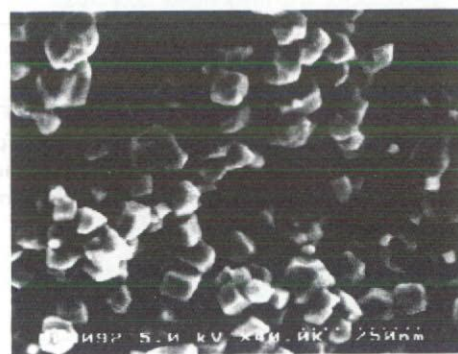

Fig. 3. SEM micrograph of sub-micron Fe particles synthesized in EG.

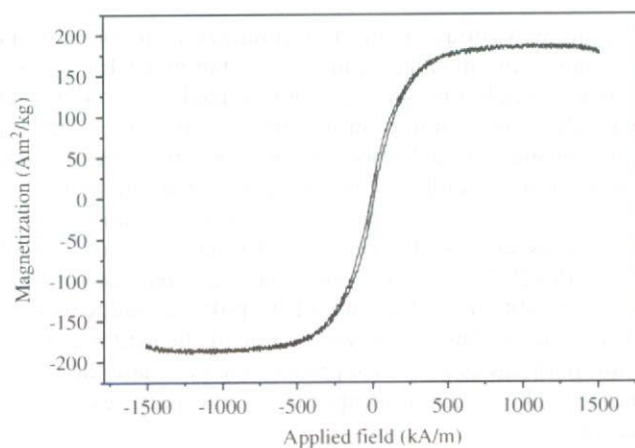Fig. 4. Hysteresis loop at room temperature for the Fe particles synthesized in EG.

reducing ability of the polyols, the yield of metal iron and iron oxide fraction in the product varied. The Fe_3O_4 fraction is the highest for the particles synthesized in TMEG, and almost no oxide peak is visible for the particles synthesized in EG as shown in Fig. 1. The particle size for the Fe synthesized in EG and TMEG are around 100 and 60 nm as observed from SEM and TEM (not shown), respectively. The larger particle size confirms that the particles are polycrystalline since the grain sizes observed from the XRD pattern are much smaller. The results suggest that the formation of oxides is due to the oxidation of iron and their fraction is related to the size of the nanoparticles. The highly reducing TMEG gives rise to the formation of smaller particles, which subsequently gets oxidized. On the other hand, the Fe particles synthesized in EG are large in diameter and the oxide fraction is below the detection limit of XRD. This has also been confirmed from the magnetic properties of the products. The saturation magnetizations for the particles synthesized in TMEG, PG and EG are 70, 82 and 126 A m^2/kg, respectively. The saturation magnetization is higher than that of magnetite nanoparticles (60 A m^2/kg) but less than that of bulk Fe (220 A m^2/kg). The magnetization value lower than the bulk is due to the distribution in the particle sizes with smaller particles getting converted to magnetite resulting in the reduction of magnetization. The yield and particle size of Fe synthesized in polyols varied depending on the reduction potential of the polyols. This suggests that the reaction mechanism for the formation of Fe nanoparticles in polyols is by reduction and not through disproportionation, where reaction does not depend upon the type of polyols. To confirm this further, we attempted the synthesis of iron particles in EG under various experimental conditions.

3.2. Synthesis of Fe in EG

As mentioned earlier, since the distribution of particles with smaller sizes would result in the oxidation of Fe, the reaction parameters such as OH$^-$/Fe ratio, temperature and heating rate were varied to obtain highly pure Fe particles. Among these, NaOH is found to play a major role in reducing any metal ion to metal atom. In the present case, the excess OH$^-$ helps in reducing the reduction potential, E_h, of the species [3] as well as enhances the reaction rate by facilitating the formation of acetaldehyde. The XRD pattern of the product obtained under optimum conditions is shown in Fig. 2. Fig. 3 shows the typical SEM

micrograph of Fe particles obtained above. The shape of the sub-micron size particles is found to be cubic. Fig. 4 shows the hysteresis loop at room temperature for the Fe particles synthesized in EG. The saturation magnetization of the particles is as large as $182.5 \, A \, m^2/kg$ suggesting that the oxide fraction was very low. The absence of magnetite, which should be present in equal amount in the case of disproportionation reaction, suggests that the particles are produced through the reduction of iron ions into metal as in the cases of reducing any other noble or transition metals.

4. Conclusion

We could conclude that the polyol acts as a reducing agent rather than a medium for the disproportional reaction as claimed earlier. The oxide peak appears in the Fe nanoparticles synthesized by polyol process due to the oxidation of smaller iron particles. The magnetic properties of the Fe nanoparticles are thus influenced by the particle size, where the smaller particles undergo oxidization and thereby the overall saturation magnetization is reduced. The synthesis of Fe at low temperatures will pave the way for Fe-based alloy nanoparticles such as FePt and FeCo with better magnetic properties at low temperatures.

References

[1] G. Viau, F. Fievet-Vincent, F. Fievet, J. Mater. Chem. 6 (1996) 1047.
[2] B. Jeyadevan, A. Hobo, K. Urakawa, C.N. Chinnasamy, K. Shinoda, K. Tohji, J. Appl. Phys. 93 (2003) 7574.
[3] F. Fievet, F. Fievet-Vincent, J.P. Lagier, B. Dumont, J. Mater. Chem. 3 (1993) 627.

Synthesis of size-controlled Fe–Co alloy nanoparticles by modified polyol process

D. Kodama[a,*], K. Shinoda[b], K. Sato[c], Y. Sato[a], B. Jeyadevan[a], K. Tohji[a]

[a]Graduate school of Environmental Studies, Tohoku University, Sendai, Miyagi 980-8579, Japan
[b]Institute of Multidisciplinary Research for Advanced Materials, Tohoku University, Sendai, Miyagi 980-8577, Japan
[c]Dowa Mining Company, Chiyoda, Tokyo 110-8282, Japan

Abstract

Recently, the authors have demonstrated the successful synthesis of Fe–Co nanoparticles with various compositions by using polyol process. In this paper, the synthesis of Fe–Co nanoparticles with their sizes varying between 200 and 35 nm were reported. This was achieved by tuning experimental parameters such as hydroxyl ion and metal ion concentrations, which control the nucleation and growth processes of the system.

© 2006 Elsevier B.V. All rights reserved.

PACS: 74.25.Ha; 75.50.Bb; 75.50.Tt

Keywords: Polyol process; Fe Co nanoparticle; Soft magnetic material

1. Introduction

The bulk Fe–Co alloy is used in various engineering applications due to their good, soft magnetic properties [1]. Though the use of soft magnetic Fe–Co nanoparticles in engineering applications is envisaged, the potential of the same is yet to be explored fully due to their unavailability. Recently, the authors have succeeded in the synthesis of pure Fe–Co alloy particles with varying concentrations of iron, using a modified polyol process [2]. In this paper, we present the synthesis scheme to produce Fe–Co alloy nanoparticles of various sizes by reducing the metal ions by polyol.

2. Experimental

Fe–Co alloy nanoparticles were prepared by dissolving $FeCl_2 \cdot 4H_2O$ and $Co(acetate)_2 \cdot 4H_2O$, NaOH and PVP in 100 ml ethylene glycol and the solution was heated up to 403 K. The reaction vessel was refluxed for 3 h while

stirring. Finally, the suspension was cooled down to RT. The products were recovered from polyol and washed with ethanol. The morphology, composition, structure and magnetic properties of the products were analyzed by SEM, XRF, XRD and VSM.

3. Results and discussion

The physical properties of the particles synthesized by polyol process depend on the reaction rate of the reduction process. In polyol process, the reduction rate of metal ions is a function of various experimental parameters described by the equation given below:

$$r = f(P_{redox}, C_{metal}, C_{OH}, T).$$

Here, P_{redox} is the reduction potential of polyol, C_{metal} the metal ion concentration, C_{OH} the concentration of hydroxyl ions, and T the reaction temperature. The metal formation consists of nucleation and growth stages, which depend on the reduction rate [3]. The particles become smaller when the nucleation stage becomes predominant during the synthesis of the particle. On the other hand, when the growth process becomes dominant, bigger

*Corresponding author. Tel.: 022 795 7392.
E-mail address: kodama@buckyl.kankyo.tohoku.ac.jp (D. Kodama).

particles are obtained. Though the nucleation and growth steps are very much influenced by P_{redox}, C_{metal}, C_{OH} and T, which influence the reaction rate of the process, the control of the size of Fe–Co alloy nanoparticles was attempted by tuning the experimental parameter such as metal and hydroxyl ion concentrations. To understand the influence of the above parameters, experiments were carried out by (i) varying the metal ion concentration for a fixed hydroxyl ion concentration and (ii) varying hydroxyl ion concentration for a fixed metal ion concentration.

Fig. 1 shows the XRD spectra of Fe–Co particles synthesized at metal ion concentrations of 0.07 (sample A), 0.05 (sample B) and 0.02 (sample C) mol/l, for a fixed hydroxyl ion concentration of 2 mol/l. It is seen from Fig. 1, that the diffraction lines corresponding to Fe–Co alone were recorded. The peak width of sample C was comparatively broader than samples A and B. The average grain size of samples A–C determined using Scherer's equation were 35, 33 and 21 nm, respectively. However, the size of particles in samples A–C, estimated from the SEM micrograph shown in Fig. 2, are about 150, 100 and 35 nm, respectively. This suggests that the particles in all the samples are polycrystalline in nature.

Since the size control was attempted by fixing the reaction temperature and concentration of protective agent (PVP), which control the degree of agglomeration and shape of the particles, the decrease in particle size with the decrease in metal ion concentration could be explained as follows. The number of nucleus formed during the reaction is determined by the hydroxyl ion concentration. Thus, the amount consumed for the formation of the nucleus will remain constant irrespective of the metal ion concentration above the critical value (metal concentration consumed for nucleation). Thus, the amount of metal ions available for growth varies with the metal ion concentration. This consequently leads to the variation in particle size. Thus, bigger particles will be formed at higher metal ion concentration.

Similarly, the particle size could also be controlled by fixing the metal ion concentration and varying the hydroxyl
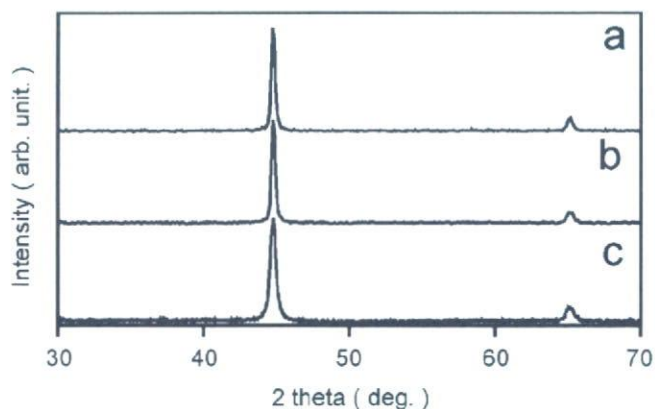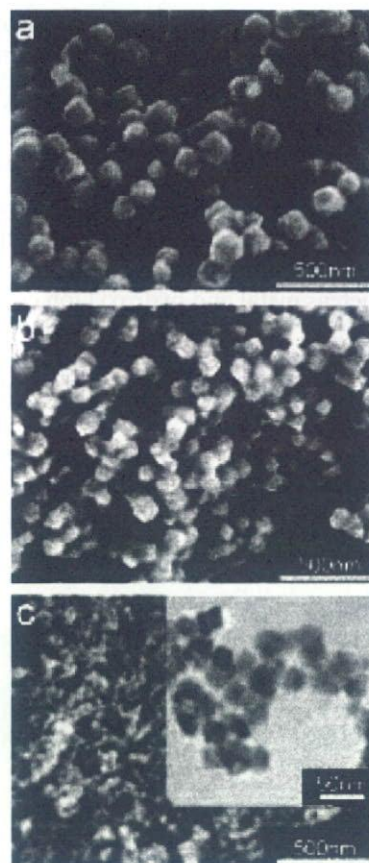

Fig. 2. SEM micrographs of Fe Co particles in samples (a) A, (b) B and (c) C (inset shows the TEM micrograph).

ion concentration. When the hydroxyl ion concentration is below a critical value, the reduction rates of Fe and Co ions became low and the product consisted of intermediate phases beside Fe–Co alloy. Furthermore, the particles exhibited broad size distributions. The above results suggested that, there exists a critical hydroxyl ion concentration for the synthesis of pure Fe–Co particles. When the concentration of hydroxyl ion is increased above the critical concentration, the particle size began to decrease. This also confirmed that the hydroxyl ion concentration determines the rate at which the nuclei are formed. Therefore, when the number of nuclei formed increases with increasing hydroxyl ion concentration, the metal ions left for growth of the nucleus become lesser and consequently, the particle size becomes smaller. However, when the hydroxyl ion concentration becomes very strong, the particles coagulate to form large aggregates. The particle size range obtained using the above technique was 200–50 nm. Though the particles synthesized at higher hydroxyl ion concentration were strongly aggregated, the grain size was comparable to the one obtained varying the metal ion concentration. Though the polydispersity as well as variation in composition from particle to particle cannot be ruled out completely, the SEM

Fig. 1. XRD profiles of samples (a) A, (b) B and (c) C.

observation as well as Mossbauer spectroscopic analysis suggested that variation in size distribution and composition are minimum.

4. Conclusion

The synthesis technique to obtain size controlled Fe–Co nanoparticles has been successfully developed by manipulating the nucleation and growth steps with experimental parameters such as metal and hydroxyl ion concentrations.

Consequently, Fe–Co nanoparticles with sizes ranging between 200 and 35 nm were achieved.

References

[1] Y.G. Chin, H.J. Wernich, in: E.P. Wohlfarth (Ed.), Ferromagnetic Materials, North-Holland, Amsterdam, 1980.
[2] D. Kodama, K. Shinoda, K. Sato, Y. Sato, B. Jeyadevan, K. Tohji, Intermag 2006.
[3] T. Sugimoto, F. Shiba, T. Sekiguchi, H. Itoh, Colloids Surf. A 164 (2000) 183.

Heating efficiency of magnetite particles exposed to AC magnetic field

Takashi Atsumi[a,*], Balachandran Jeyadevan[b], Yoshinori Sato[b], Kazuyuki Tohji[b]

[a]*Ferrotec corporation, 1-4 Midoridaira, Sosa, Chiba 289-2131, Japan*
[b]*Tohoku University, 6-6-20 Aramaki aza aoba, Aoba-ku, Sendai 980-8579, Japan*

Available online 27 November 2006

Abstract

Magnetic hyperthermia is a type of cancer treatment that utilizes the heat generated from magnetic particles to destroy cancer cells selectively. The heating efficiency depends strongly on the magnetic properties of the particles. In this paper, we experimentally verify the heat generation efficiency of magnetite particles of various diameters and propose the properties of magnetite particles suitable for magnetic hyperthermia.
© 2006 Elsevier B.V. All rights reserved.

PACS: 87.54.Br; 75.50.Mm

Keywords: Hyperthermia; Superparamagnetic nanoparticle; Coprecipitation method; Heat efficiency

1. Introduction

Magnetic hyperthermia is a type of cancer treatment proposed to increase the temperature of the body tissue above 42 °C using the heat generated from magnetic particles. The heating effect depends strongly on the magnetic properties of the particles, which may vary appreciably depending on their size and microstructure. Though this has been proposed in the beginning of the 20th century, the recent technological advancement in nano-particle synthesis has renewed the interest among researchers. In this paper, we discuss the properties of magnetic particle suitable for cancer therapy under magnetic field strength and frequency conditions considered safe for humans. Then, we report the chemical synthesis techniques to obtain the magnetic particles with suitable properties. Finally, the heat dissipation efficiency of magnetic suspensions with different particle diameters and size distribution is reported and discussed.

2. Magnetic particles suitable for hyperthermia

The magnetite particles can be either ferromagnetic or superparamagnetic at room temperature depending on their diameter. The critical diameter of magnetite has been evaluated to be 18.7 nm assuming the crystalline anisotropy constant to be $30 \, kJ/m^3$. Heat can be generated by both ferromagnetic and superparamagnetic particles exposed to AC magnetic field. However, considering the magnetic field intensity and AC frequency range that could be used during treatment, superparamagnetic particles have been proved to be effective [1,2].

The magnetic vector of single domain particle relaxes through either Brownian or Néel relaxation depending on the anisotropy and size of the particle. Considering the operational AC frequency range, and magnetic field strength for hyperthermia treatment, the power dissipation depends on the AC susceptibility of the particle, which is a function of the particle diameter. Though the heat dissipation would increase with particle diameter for a fixed AC frequency, the particle remains superparamagnetic only below a specific diameter [2]. When the particle diameter is larger than the superparamagnetic limit, the particles become ferromagnetic and the heat is dissipated only when the external magnetic field strength is larger than the coercive force for any given frequency. However, it should be noted that the coercivity of ferromagnetic particles increase with frequency and the external field necessary to generate hysteresis loss becomes larger. On the contrary, superparamagnetic particles generate heat at
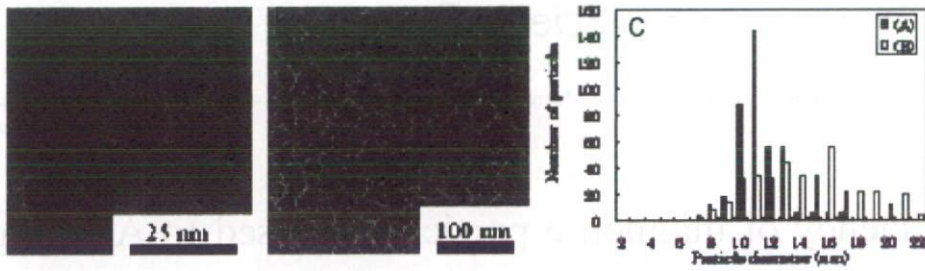

Fig. 1. TEM photographs of magnetite samples for the particles synthesized by (a): thermal decomposition, and (b) coprecipitation techniques and their corresponding size distribution (c).

comparatively lower magnetic field strength. Thus, the use of superparamagnetic particles is favored over ferromagnetic particles and the type of magnetic material and properties suitable for hyperthermia treatment has already been analyzed theoretically [1,2]. Magnetite particles with diameters lying between 11 and 13 nm are considered suitable to generate considerable heat from particles exposed to an alternating magnetic field of 3.2 kA/m and frequency of 600 kHz. Furthermore, the efficiency of power dissipated from superparamagnetic particles is enhanced further when the particles' size distribution is narrow [1].

3. Synthesis of magnetite particles

The synthesis of magnetite particles with various diameters was attempted by the thermal decomposition method and coprecipitation combined with the size classification methods [1]. The corresponding SEM micrographs are shown in Figs. 1(a) and (b) respectively. Particles with average diameter 11 nm and narrow size distribution were synthesized by controlling the reaction parameters such as surfactant concentration, reaction time, etc. using the thermal decomposition technique designated as sample A (Fig. 1(a)). Though the particles synthesized by coprecipitation exhibited wide size distribution, subsequent size classification enabled the preparation of a sample that was free of particles with less than 8 nm and had an average diameter of 14 nm designated as sample B (Fig. 1(b)). It should be noted that sample A, which has a large fraction of particles with diameters closer to the optimum diameter predicted by theory, is expected to dissipate more heat than sample B.

4. Evaluation of heat dissipation capacity of magnetic particles

Heat dissipation of magnetic particles was evaluated by using an AC magnetic field generator whose maximum magnetic field intensity and frequency are 3.2 kA/m and 600 Hz, respectively. The heat generated from samples A and B was evaluated by exposing 3 ml of 4 wt% magnetic particle suspension dispersed in isoparaffin to an AC
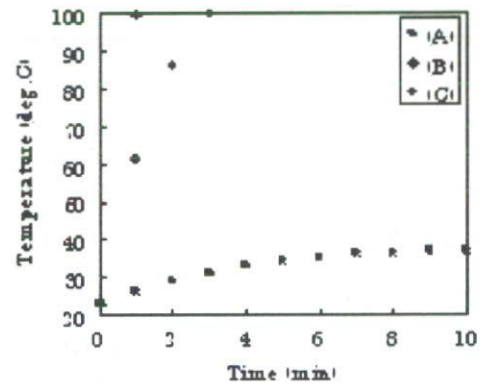

Fig. 2. Temperature of magnetite suspensions against AC magnetic field exposure time for (A) sample A and (B) sample B (C) unclassified coprecipitated samples.

magnetic field. The details of the experimental setup are described elsewhere [1]. The temperature of magnetite particle suspensions against exposure time is shown in Fig. 2. The temperature of sample A rose over 100 °C in about a minute, whereas the temperature of sample B rose gradually against time and the heat dissipated was well below that of sample A.

Though the microscopic observation provides information on the morphology of the particles, AC susceptibility measurements were necessary to understand the heat dissipation behavior of the samples. The AC susceptibility measurements of samples A and B are given in Fig. 3. The maximum susceptibility of sample A was at 170 K and sample B exhibited the maximum in the vicinity of room temperature, whereas the unclassified coprecipitated sample recorded the maximum at 190 K. Thus, more number of particles in sample B will respond to the AC field and generate heat than in sample A. This behavior is in agreement with the results of the heat dissipation experiment carried out at room temperature. The higher blocking temperature of sample B can be due to either the presence of particles larger than 14 nm and/or magnetic interaction of the particles. Further investigation is necessary to understand the individual contribution of the factors.

a

b
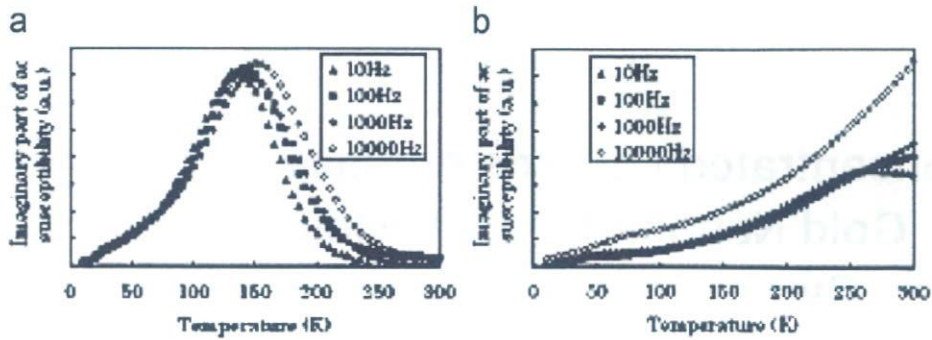
Fig. 3. Measurement results of imaginary part of ac susceptibility for (a) sample A and (b) sample B.

5. Summary

The magnetite particle suitable for hyperthermia was investigated. The dependence of particle diameter in heat dissipation was experimentally verified. Maximum heat dissipation was observed for the suspension with an average particle diameter of 14 nm synthesized by the coprecipitation method.

Furthermore, the removal of particles smaller than 8 nm proved vital in improving the heating efficiency of the magnetic suspension dispersed with magnetite particles synthesized by coprecipitation.

References

[1] T. Atsumi, B. Jeyadevan, Proc. SPIE. Int. Soc. Opt. Eng. 628 (2002) 5593.
[2] R.E. Rosensweig, J. Magn. Magn. Mater. 252 (2002) 370.

Concentrated Colloids of Silica-Encapsulated Gold Nanoparticles: Colloidal Stability, Cytotoxicity, and X-ray Absorption

Yeon-Su Park[1, *], Atsuo Kasuya[1, *], Andriy Dmytruk[1], Noda Yasuto[1], Motohiro Takeda[2], Noriaki Ohuchi[3], Yoshinori Sato[4], Kazuyuki Tohji[4], Motohiro Uo[5], and Fumio Watari[5]

[1] Center for Interdisciplinary Research, Tohoku University, Aoba-ku, Sendai 980-8578, Japan
[2] Department of Bioengineering and Robotics, Tohoku University, Aoba-ku, Sendai 980-8579, Japan
[3] Division of Surgical Oncology, Graduate School of Medicine, Tohoku University, Aoba-ku, Sendai 980-8574, Japan
[4] Graduate School of Environmental Studies, Tohoku University, Aoba-ku, Sendai 980-8579, Japan
[5] Graduate School of Dental Medicine, Hokkaido University, Kita-ku, Sapporo 060-8589, Japan

As an effort to develop a new, effective, nontoxic X-ray contrast agent, the concentrated colloids of silica-encapsulated gold nanoparticles (Au@SiO$_2$ NPs) were fabricated and their colloidal stability, cytotoxicity, and X-ray absorption were investigated. The concentrated colloidal NPs were manufactured by forming a 4 nm-thick silica shell on the surface of each Au NP with 15 nm diameter, followed by enrichment to [Au] = 100 mM. They were very stable in water: the NPs were well separated each other without forming agglomerates and their optical property was very similar to that before enrichment. The colloidal stability of the NPs in biological environment was strongly dependent on their previous morphology in water. The NPs with minor shell damage were stable in phosphate buffered saline (PBS) solution: both in water and in PBS solution, they showed very similar morphology and optical property. However, the NPs with profound shell damage formed big agglomerates in PBS solution, resulting in the red-shift and broadening of the Au surface plasmon resonance peak. Cell viability and proliferation assessments revealed the biocompatibility of the Au@SiO$_2$ NPs: no apparent cytotoxicity was observed even at 100 ppm NPs. The concentrated colloidal NPs showed very strong X-ray absorption. Their relative X-ray transmittance to water was comparable to that of a commercial agent. Considering these, the concentrated colloids of the Au@SiO$_2$ NPs are suitable for an X-ray contrast agent.

Keywords: Gold, Silica, X-ray Absorption, Cytotoxicity, Colloidal Stability.

1. INTRODUCTION

As concerns on human health increase tremendously in modern society, there have been strong demands for more effective and safer medical diagnoses. One of the most indispensable modern diagnostic tools is a computed tomography (CT), which strongly relies on the contrast ability of X-ray contrast agents. Currently, tri-iodobenzene derivatives are extensively used as the contrast agents. However, sometimes these iodine-containing small organic molecules cause some serious problems such as limited imaging time, due to their short vascular circulation time, and renal toxicity. Thus, CT practices occasionally require intra-arterial catheterization which may impose serious health risks. In these regards, there have been

ceaseless efforts to develop more effective and safer X-ray contrast agents.[1-5] Most of them have focused on the modification of iodine-containing contrast molecules: encapsulation in[1-4] or linkage to[5] biocompatible organic molecules/polymers. A recent report by Hainfeld et al., however, demonstrated a possibility of Au NPs for an X-ray contrast agent.[6] They obtained the contrast images of the blood vessels and some organs of mice, by utilizing concentrated colloids of 1.9 nm diameter Au NPs as an X-ray contrast agent.

The nontoxic nature of bulk Au and relatively large (e.g., a few nm or bigger in diameter) Au NPs has been well documented,[7, 8] but investigations on the toxicity of small Au NPs have been scarce. Recently, Schmit et al. reported the toxicity of very small Au NPs.[9, 10] The authors observed strong cytotoxicity from 1.4 nm Au NPs, of which size is in a range for deteriorative interaction with

the major grooves of deoxyribonucleic acids (DNAs). Thus, for medical applications, it is highly desirable to use the Au NPs larger than DNA grooves (typically less than 2 nm). In addition to the cytotoxicity problem, the Au NPs commensurate with or smaller may cause poor X-ray contrast because of their short vascular circulation time. However, very large Au NPs are also undesirable for medical applications because of the colloidal stability of the NPs decreasing with size and the difficulty in preparing homogeneous large (e.g., 40 nm or bigger in diameter) Au NPs.[11] Taking these into account, relatively large (here, between 10 and 40 nm in diameter) Au NPs seem to be suitable for an X-ray contrast agent application.

Like many medical applications of other colloidal NPs, the application of colloidal Au NPs for an X-ray contrast agent requires them being in a highly concentrated state to ensure high X-ray contrast. However, it is not a trifle to prepare stable and concentrated colloids of relatively large Au NPs, without proper surface modifications, because of their strong tendency to coagulate in concentrated state. One of the most useful and bio-friendly surface modifications is to encapsulate each Au NP in a silica shell because silica is biocompatible, feasible for further surface modifications,[8, 12–14] and has strong negative charge in biological environment.[15] The strong negative charge on the silica surfaces, contributing to electrostatic repulsion among the NPs, may enable to prepare highly stable and concentrated colloids of relatively large Au NPs.

There has been sparse documentation[16] on the concentrated colloids of silica-encapsulated Au (Au@SiO_2) NPs, even though plenty of documents[12, 17–22] have been available on the morphology and optical property of the NPs and their assemblies prepared from relatively low precursor concentration without enrichment. Unfortunately, no documentation is available on the colloidal stability and cytotoxicity of Au@SiO_2 NPs in biological environment, which are essential factors for medical applications. Here, as an effort to develop a new class of an effective and safe X-ray contrast agent, we report the colloidal stability in biological environment, *in vitro* cytotoxicity, and X-ray absorption of the concentrated colloidal Au@SiO_2 NPs (Au core diameter = ca. 15 nm, silica shell thickness = ca. 4 nm), along with their morphology and optical property.

2. EXPERIMENTAL DETAILS

2.1. Materials

Hydrogen tetrachloroaurate(III) tetrahydrate (HAuCl_4·4H_2O), trisodium citrate dehydrate (Na_3-Cit), formaldehyde, 0.1 M phosphate buffered saline (PBS) solution were purchased from Wako Pure Chemicals. 3-Aminopropyl trimethoxysilane (APS) was supplied by Alfa-Aesar. Sodium silicate solution (ca. 27% SiO_2), DOWEX® 50WX4-400 ion-exchange resin, alpha-Minimum Essential

Medium (MEM), and fetal bovine serum (FBS) were acquired from Sigma-Aldrich. Trypan blue and alamarBlue™ were provided by Gibco and Biosource, respectively. All chemicals were used as received. Milli-Q water (>18.2 MΩ cm) was used to prepare all aqueous solutions.

2.2. Preparation

The colloids of citrate-stabilized Au NPs were prepared according to the previously reported procedure.[11, 16] Briefly, 15 ml of mildly heated 1% Na_3-Cit solution was added to 282 ml of boiling 0.532 mM HAuCl_4·4H_2O solution under stirring: the final concentrations of Au^{3+} and citrate^- were 0.5 and 0.17 mM, respectively. Silica shells were formed by adding 0.75 ml of 1 mM APS solution and 12 ml of 0.54 wt% sodium silicate solution (pH = 10.5–11, adjusted by using DOWEX® 50WX4-400 ion-exchange resin) to 300 ml of the colloids of citrate-stabilized Au NPs, followed by standing the mixtures (pH ≅ 8.5) for three days.[14, 16, 17, 21] The resulting colloids of Au@SiO_2 NPs were cleaned by a series of washing cycle: centrifugation (25,000 × g, 15 minutes), supernatant removal, and redispersion in water. Concentrated colloids were prepared by repeating the washing cycle, while gradually decreasing the amount of water for redispersion in each cycle (hereafter, referred as a 'mild enrichment'). A typical mild enrichment consisted of 4 washing cycles. Assuming that all Au^{3+} ions were used for producing Au NPs, the concentration of metallic Au in the concentrated colloids was 100 mM, 200 times higher than that in the colloids before the enrichment. Twice repetition of the mild enrichment was also performed to investigate its influence on the morphology and optical properties of the NPs. In this case, the final concentration of metallic Au in the resulting colloidal solution was also adjusted to 100 mM. For convenience, the metallic Au concentration was used for representing the concentration of Au or Au@SiO_2 NPs in colloids.

2.3. Instrument and Characterization

For characterizing the morphology of the NPs, the transmission electron microscopy (TEM) was performed with a JEOL JEM-2000 microscope operating at 200 KeV. The optical property of the colloidal NPs was characterized from their visible absorption spectra obtained with a Hitach U-2000 spectrophotometer. All optical spectra were obtained after adjusting metallic Au concentration to 0.5 mM. A Rigaku Rotaflex X-ray spectrometer was used for measuring X-ray transmittances of samples.

The stability of the concentrated colloidal NPs in biological environment was characterized based on the changes in their morphology and optical property upon transferring to 0.1 M PBS solution. The volume ratio of the colloid to the PBS solution was set to 0.5.

The viability and proliferation of rat fibroblast MC3T3-E1 cells, assessed by using a almarBlue™ assay, were used for evaluating the cytotoxicity of the NPs. For cell viability tests, the rat fibroblasts were incubated at 37° in 24-well plates using alpha-MEM containing 10% FBS (10^4 cells per well) and then various amount of the NPs (0.01–100 ppm) in water were added to each well. After further incubation at 37° for 24 hours, the viability of the rat fibroblasts was estimated based on the calorimetric detection of almarBlue™ reduction caused by live cells. For cell proliferation assays, both the rat fibroblasts and the NPs in water were seeded onto 24-well plates using alpha-MEM containing 10% FBS (10^4 cells per well) and then co-incubated for 24 hours. After cell fixing with formaldehyde and staining with trypan blue, stained cells (live cells) were counted under an optical microscope. In both the tests, the control sample was rat fibroblast MC3T3-E1 cells.

3. RESULTS AND DISCUSSION

3.1. Morphology

The citrate-induced reduction of Au^{3+} produced homogeneous spherical Au NPs with ca. 15 nm in diameter (Fig. 1(a)). The Au@SiO$_2$ NPs, prepared through silica coating in the basic silicate solution, are well separated
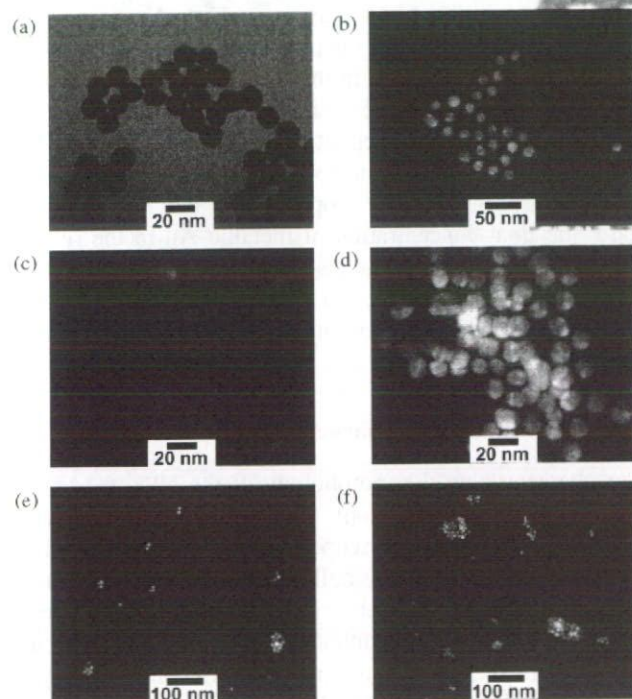
each other without forming agglomerates, as shown in Figure 1(b). They have relatively homogeneous spherical silica shells of which thickness is ca. 4 nm.

The concentrated colloidal Au@SiO$_2$ NPs, prepared through the mild enrichment, are well separated each other without forming agglomerates, even though some silica shells have minor shell damage such as detachment of some silica (Fig. 1(c)). The stability of these concentrated colloidal Au@SiO$_2$ NPs with minor shell damage (MSD) can be attributed to their high surface charge. In the experimental conditions of near neutral pH, the silica surfaces have high negative charge owing to the low isoelectric point of silica.[15] This enhances electrostatic repulsion among the NPs enough to stabilize them in the concentrated state.

The repetition of the mild enrichment exerted detrimental effect on the morphology of the Au@SiO$_2$ NPs. As shown in Figure 1(d), twice repetition of the enrichment resulted in profound shell damage (PSD): the silica shells seem to be inhomogeneous and little compact, compared with those obtained through the typical mild enrichment process; in part, they are loosely distributed among the Au NPs. Most of the NPs with PSD are poorly separated each other. In many cases, each NP is closely contacting with its immediate neighbor NPs through very thin silica barrier. Some NPs partially expose their Au cores or have big cores compose of two or more Au NPs. The formation of the big cores is related with the coagulation of the NPs with no or little silica. They have surface charge insufficient to prevent them from coagulation, because their surface charge diminishes with decreasing silica surface area.

3.2. Optical Property

As shown in Figures 2(a) and (b), the formation of 4 nm-thick silica shells caused a shift of Au surface plasmon resonance (SPR) peak from 519 to 523 nm. This red-shift by 4 nm is due to an increase in the local refractive index of the surrounding medium[17, 22] and is well in accordance with previous reports.[16, 17]

The optical property of the Au@SiO$_2$ NPs was strongly dependent on their morphology. As shown in Figure 2(c), the NPs with MSD show a SPR peak of which shape, intensity, and position are very similar to those of the NPs before the enrichment (Fig. 2(b)). The SPR peak of the NPs with PSD in Figure 2(d), however, is somewhat broad, weak, and red-shifted by 3 nm, compared with that of the NPs with MSD. These slight changes in optical property can be attributed to the close contact of the NPs and the existence of the NPs with bigger Au core.

3.3. Colloidal Stability in Biological Environment

In biological environment, the concentrated colloidal Au@SiO$_2$ NPs formed agglomerates of which size was strongly dependent on their initial morphology in water.

Fig. 1. TEM images of Au and Au@SiO$_2$ nanoparticles: (a) citrate-capped Au, (b) as-prepared Au@SiO$_2$ in water, (c) Au@SiO$_2$ in water after mild enrichment, (d) Au@SiO$_2$ after twice repetition of mild enrichment, (e) Au@SiO$_2$ in 0.1 M PBS solution after mild enrichment, and (f) Au@SiO$_2$ in 0.1 M PBS solution after twice repetition of mild enrichment. The concentrations of the NPs before and after the enrichments were equivalent to 0.5 and 100 mM metallic Au, respectively.
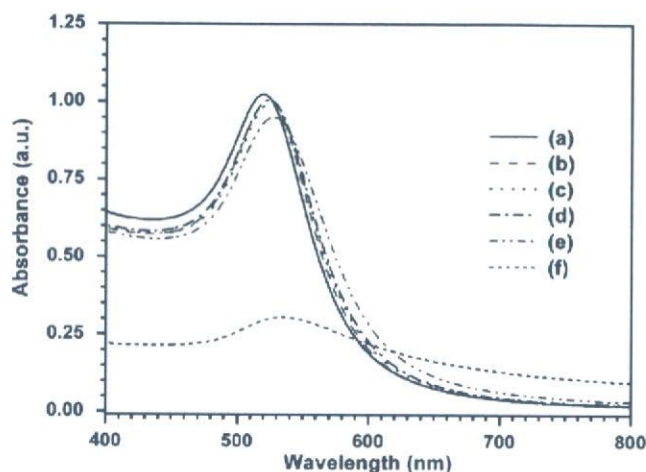
Fig. 2. Visible absorption spectra of Au and Au@SiO₂ nanoparticles: (a) citrate-capped Au, (b) as-prepared Au@SiO₂ in water, (c) Au@SiO₂ in water after mild enrichment, (d) Au@SiO₂ after twice repetition of mild enrichment, (e) Au@SiO₂ in 0.1 M PBS solution after mild enrichment, and (f) Au@SiO₂ in 0.1 M PBS solution after twice repetition of mild enrichment.

As shown in Figure 1(e), the morphology of the NPs with MSD in the PBS solution is very similar to that of the corresponding NPs in water, except for some agglomerates composed of relatively small number of the NPs. The formation of slightly more and bigger agglomerates of the NPs in the PBS solution is related with the flocculation caused by an increase in the ionic strength of the solution. Due to its high ion concentration, the PBS solution has stronger ionic strength than water. As the ionic strength of a solution increases, charge (opposite in sign) density around NPs increases. Because both ionic strength and charge density are inversely proportional to the square of the Debye shielding length, which is a measure of the strength of electrostatic potential damping from its pure value, electrostatic repulsion among the NPs is reduced and hence the NPs are destabilized with increasing ion concentration. Unlike those with MSD, the concentrated colloidal Au@SiO₂ NPs with PSD were unstable in the PBS solution: an immediate formation of precipitates was observed upon transferring to the solution. As shown in Figure 1(f), the TEM images of the NPs with PSD in the PBS solution show big agglomerates, along with some single NPs and small agglomerates composed of a few NPs with little or no silica shell. The big agglomerates consist of a few tens of the NPs, in which a couple of bigger Au NP cores are included. As discussed earlier, the formation of the big agglomerates of the NPs with PSD is related with the ionic strength of the PBS solution.

The optical property of the Au@SiO₂ NPs in PBS solution was also strongly influenced by their initial morphology: the NPs with MSD showed little change, whereas those with PSD experienced drastic change. The visible absorption spectrum of the NPs with MSD in the PBS solution (Fig. 2(e)) is very similar to that of the

corresponding NPs in water (Fig. 2(c)): there is little difference in the shape, intensity, and position of the Au SPR peak. However, as shown in Figure 2(f), the NPs with PSD in the PBS solution shows a broad and weak Au SPR peak with very large background, compared with those in water (Fig. 2(d)). And their SPR peak is located at 534 nm, which is 7 nm longer than that in water. These optical observations imply the existence of various sizes of bigger NPs in the PBS solution and are well coincided with the previously described microscopic observations.

3.4. Cytotoxity

For medical applications, the Au@SiO₂ NPs should be biocompatible. Their biocompatibility was evaluated based on the viability and proliferation of rat fibroblast MC3T3-E1 cells. In general, 50% cell viability (or proliferation) is considered as a border of live or dead cells: materials giving 50% or higher cell viability (or proliferation) are biocompatible, while those with lower than 50% values are toxic. Figure 3 shows the viability and proliferation of the rat fibroblast cells after 24 hours incubation. In all the NP concentrations tested here, the rat fibroblast cells show more than 50% viability and proliferation. Even at a very high NP concentration of 100 ppm, the cell viability and proliferation are more than 70 and 60%, respectively. These confirm the biocompatibility of the Au@SiO₂ NPs. Especially the NPs show excellent biocompatibility at the concentration of 1 ppm or lower, as can be inferred from near 100% cell viability and proliferation.

3.5. X-ray Absorption

For achieving high X-ray contrast, contrast agents should show much stronger X-ray absorption (so, much lower X-ray transmittance) than human body, because X-ray contrasting ability relies on the differences in their X-ray
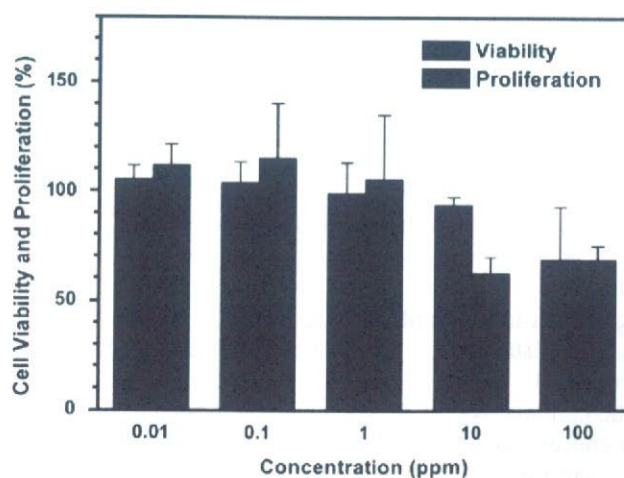

Fig. 3. Viability and proliferation of rat fibroblast MC3T3-E1 cells at various concentrations of Au@SiO₂ nanoparticles.
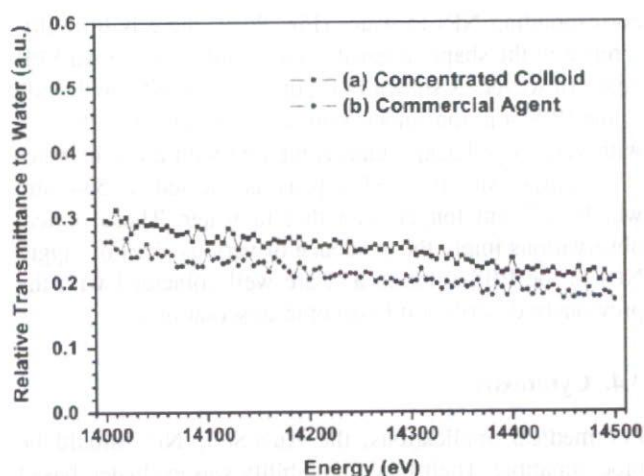
Fig. 4. Relative X-ray transmittances of (a) the concentrated colloid of Au@SiO$_2$ nanoparticles ([Au] = 100 mM) and (b) a commercial X-ray contrast agent (Iopamiron® 300). Relative transmittance = transmittance of sample/transmittance of water.

absorption. Therefore, the relative X-ray transmittance of a sample to water (a major constituent of human body) is a very important factor for evaluating its contrast ability. In general, materials with lower relative X-ray transmittance give better X-ray contrast.

Figure 4 shows the relative X-ray transmittances of the 100 mM colloidal Au@SiO$_2$ NPs and a commercial X-ray contrast agent (Iopamiron® 300). Average relative transmittance of the colloidal NPs is close to that of the commercial contrast agent. At Au L$_1$ edge, the colloidal NPs shows the relative transmittance of ca. 0.237, which is very close to the calculated value of 0.231 based on X-ray mass attenuation coefficient of Au. Their slight discrepancy may be mainly due to the loss of the NPs during enrichments. Considering very low relative X-ray transmittance, comparable to that of a commercial contrast agent, the concentrated colloidal Au@SiO$_2$ NPs may be suitable for an X-ray contrast agent application.

4. SUMMARY AND CONCLUSIONS

As an effort to develop a new class of an effective and non-toxic X-ray contrast agent, highly concentrated colloidal Au@SiO$_2$ NPs were prepared and their colloidal stability in biological environment, *in vitro* cytotoxicity, and X-ray absorption were investigated. Each NP consists of ca. 15 nm diameter Au core and ca. 4 nm thick silica shell. The concentration of the concentrated colloidal NPs was equivalent to 100 mM metallic Au.

Highly stable and concentrated colloidal Au@SiO$_2$ NPs with MSD were prepared through the mild enrichment. The colloidal NPs with MSD were morphologically stable in concentrated state: they were well-separated each other, without forming agglomerates. The optical property of the concentrated colloidal NPs with MSD was very similar to that of the colloidal NPs before the enrichment: there was

little change in the shape, intensity, and position of Au SPR peaks before and after the enrichment.

The concentrated colloidal Au@SiO$_2$ NPs with PSD were prepared through the repetition of the mild enrichment. The concentrated colloidal NPs with PSD showed the morphology somewhat different from that of the concentrated colloidal NPs with MSD: they were poorly separated each other and had very close contact with neighbor NPs. Due to their morphology, the NPs with PSD showed a Au SPR peak which is slightly broad, weak, and red-shifted as compared with that of the NPs with MSD.

In biological environment, the stability of the concentrated colloidal Au@SiO$_2$ NPs was strongly dependent on their previous morphology in water. The concentrated colloidal NPs with MSD were stable in PBS solution, even though some small agglomerates were formed. However, the concentrated colloidal NPs with PSD were unstable in PBS solution: they formed big agglomerates, resulting in precipitation. These morphological differences affected their optical property. The colloidal NPs with MSD in PBS solution showed the Au SPR peak similar to that of the NPs in water, whereas those with PSD showed a very broad and red-shifted peak in PBS solution, as compared with those in water.

The Au@SiO$_2$ NPs are biocompatible. Both cell viability and proliferation assessments revealed no apparent cytotoxicity of the NPs even at the highest NP concentration tested here (100 ppm). Especially, at 1 ppm or lower, the NPs have an excellent biocompatibility: they showed near 100% cell viability and proliferation.

The concentrated colloidal Au@SiO$_2$ NPs showed strong X-ray absorption. Their relative transmittance to water, being inversely proportional to their X-ray contrast ability, is very low and close to that of a commercial contrast agent.

Taking into account their high colloidal stability in biological environment, excellent biocompatibility, and relative X-ray transmittance comparable to a commercial agent, the concentrated colloids of the Au@SiO$_2$ NPs, with relatively large Au core and little (or no) silica shell damage, are excellent materials for X-ray contrast agents.

References and Notes

1. U. P. Schmiedl, W. Krause, J. Leike, and A. Sachse, *Acad. Radiol.* 6, 164 (**1999**).
2. V. P. Torchilin, *Adv. Drug Deliv. Rev.* 54, 235 (**2002**).
3. D. R. Vera and R. F. Mattrey, *Acad. Radiol.* 9, 784 (**2002**).
4. C.-Y. Kao, E. A. Hoffman, K. G. Beck, R. V. Bellamkonda, and A. V. Annapragada, *Acad. Radiol.* 10, 475 (**2003**).
5. V. P. Torchilin, M. D. Frank-Kamenetsky, and G. L. Wolf, *Acad. Radiol.* 6, 61 (**1999**).

6. J. F. Hainfeld, D. N. Slatkin, T. M. Focella, and H. M. Smilowitz, *Br. J. Radiol.* 79, 248 (**2006**).

7. E. E. Connor, J. Mwamuka, A. Gole, C. J. Murphy, and M. D. Wyatt, *Small* 1, 325 (**2005**).

8. Z. P. Xu, Q. H. Zeng, G. Q. Lu, and A. B. Yu, *Chem. Eng. Sci.* 61, 1027 (**2006**).

9. Y. Liu, W. Meyer-Zaika, S. Franzka, G. Schmid, M. Tsili, and H. Kuhn, *Angew. Chem., Int. Ed.* 42, 2853 (**2003**).

10. M. Tsoli, H. Kuhn, W. Brandau, H. Esche, and G. Schmid, *Small* 1, 841 (**2005**).

11. G. Frens, *Nat. Phys. Sci.* 241, 20 (**1973**).

12. E. Mine, A. Yamada, Y. Kobayashi, M. Konno, and L. M. Liz-Marzán, *J. Colloid Interf. Sci.* 264, 385 (**2003**).

13. T. Schiestel, H. Brunner, and G. E. M. Tovar, *J. Nanosci. Nanotechnol.* 4, 504 (**2004**).

14. B. Rodríguez-González, A. Sánchez-Iglesias, M. Giersig, and L. M. Liz-Marzán, *Faraday Discuss.* 125, 133 (**2004**).

15. X. Cui, W.-C. Zin, W.-J. Cho, and C.-S. Ha, *Mater. Lett.* 59, 2257 (**2005**).

16. Y.-S. Park, L. M. Liz-Marzán, A. Kasuya, Y. Kobayashi, D. Nagao, M. Konno, S. Mamykin, A. Dmytruk, M. Takeda, and N. Ohuchi, *J. Nanosci. Nanotechnol.* 6, 3503 (**2006**).

17. L. M. Liz-Marzán, M. Giersig, and P. Mulvaney, *Langmuir* 12, 4329 (**1996**).

18. F. Caruso, M. Spasova, V. Salgueiriño-Maceria, and L. M. Liz-Marzán, *Adv. Mater.* 13, 1090 (**2001**).

19. F. García-Santamaría, V. Salgueiriño-Maceria, C. López, and L. M. Liz-Marzán, *Langmuir* 18, 4519 (**2002**).

20. Y. Yang, M. Hori, T. Hayakawa, and M. Nogami, *Surf. Sci.* 579, 215 (**2005**).

21. I. Tunc, S. Suzer, M. A. Correa-Duarte, and L. M. Liz-Marzán, *J. Phys. Chem. B* 109, 7597 (**2005**).

22. S. Liu and M. Han, *Adv. Funct. Mater.* 15, 961 (**2005**).

AMERICAN
SCIENTIFIC
PUBLISHERS

Novel Method to Evaluate the Carbon Network of Single-Walled Carbon Nanotubes by Hydrogen Physisorption

Shinya Iwata,[†] Yoshinori Sato,[*,‡] Kouta Nakai,[†] Shohei Ogura,[†,§] Tatsuo Okano,[†,§]
Masaru Namura,[‡,ǁ] Atsuo Kasuya,[⊥] Kazuyuki Tohji,[‡] and Katsuyuki Fukutani[*,†,§]

*Institute of Industrial Science, The University of Tokyo, Komaba, Meguro-ku, Tokyo 153-8505, Japan,
CREST-JST, Komaba, Meguro-ku, Tokyo 153-8505, Japan, Graduate School of Environmental Studies,
Tohoku University, Aoba 6-6-20, Aramaki, Aoba-ku, Sendai 980-8579, Japan, Manufacturing Technologies
Department, Dowa Holdings Co., Ltd., Sotokanda 4-14-1, Chiyoda-ku, Tokyo, 101-0021, Japan, and Center for
Interdisciplinary Research, Tohoku University, Aoba 6-3, Aramaki, Aoba-ku, Sendai 980-8578, Japan*

Received: August 5, 2007; In Final Form: September 1, 2007

Physical and chemical properties of single-walled carbon nanotubes (SWCNTs) are sensitive to the defects
in the tubular graphene. To date, however, the method to characterize the defect of SWCNTs has been limited
to transmission electron microscopy (TEM) and atomic force microscopy (AFM), which can only be used to
observe the local structure of SWCNTs. In an effort to explore the evaluation method of SWCNTs, physisorption
of H_2 on high-quality SWCNTs was investigated by cryogenic thermal-desorption spectroscopy (cryo-TDS),
which revealed particular sensitivity to the defects of SWCNTs. TDS showed a sharp desorption peak at 20
K (α) for as-purified SWCNTs, and additional desorption signals were observed at 27 and ~24 K (β and γ)
for air-oxidized SWCNTs. The α, β, and γ peaks were attributed to H_2 at the groove site and interstitial
channel of a SWCNT bundle and inside of SWCNT, respectively. The sharpness of the α peak and the ratio
of α to β and γ were found to depend strongly on the sample preparation condition. With this cryo-TDS
technique, the perfectibility of the carbon network of SWCNTs can be reliably and sensitively evaluated.

Single-walled carbon nanotubes (SWCNTs) composed of a cylindrical graphene reveal depending on their chirality a variety of electronic,[1-3] mechanical,[4,5] and chemical properties.[6] A particular feature of SWCNTs is that they should be identified as "surface materials" in such a sense that their characteristics are strongly affected by the gas adsorption,[7] structural and topological defects of the tube walls including vacancies,[8] coalescence,[9] elemental substitution,[8,10] and rehybridization of the carbon bonds due to addition of functional groups.[6,11] Often encountered in the literature[12] is a large scatter in the experimental data for differently prepared SWCNTs, which can be attributed to defects and/or modification of the carbon network of SWCNTs. Because defects are readily formed during the synthesis and purification of SWCNTs,[13] evaluating the perfectibility of the carbon network is particularly important for the studies of SWCNTs. Nevertheless, characterization methods of SWCNTs have been limited to date, e.g., Raman scattering spectroscopy probing the vibrational modes at defects[14] in a rather insensitive way and nanoscopic techniques like high-resolution transmission electron microscopy (HRTEM)[15,16] and atomic force microscopy (AFM)[17,18] that can only be applied to observation of the local structure of SWCNTs.

The smallest molecule of hydrogen is physisorbed on the surfaces of SWCNTs, and the physisorption energy is expected to depend sensitively on the local carbon structure. Recent theoretical calculations in the density functional formalism and molecular dynamics using empirical potentials showed that the physisorption energy of H_2 onto inside and outside walls of a SWCNT is higher and lower than that on a flat graphene, respectively.[19-25] Although some experimental studies suggest enhancement of the physisorption energy,[26-30] the physisorption energy and site on SWCNTs are yet to be elucidated. Considering that the van der Waals force includes nonlocal and long-ranged interactions, on one hand, accurate description of the hydrogen physisorption is a great challenge to the current theory. On the other hand, hydrogen physisorption can be used to probe the carbon network structure of SWCNTs. In an effort to accurately measure the physisorption energy, we have developed a cryogenic thermal-desorption spectroscopy (cryo-TDS) apparatus and applied it to hydrogen molecules physisorbed on structurally controlled SWCNTs. We found three distinct features from 20 to 27 K in the spectrum and determined the H_2 physisorption energy from each peak. On the basis of the experimental data, we discuss the adsorption site of hydrogen molecules on SWCNTs. By applying this cryo-TDS technique to various SWCNTs, furthermore, we found that H_2 TDS is particularly sensitive to the network of SWCNT, which definitely enables us to characterize the perfectibility of SWCNTs.

SWCNTs were synthesized by a direct-current arc-discharge method in He gas with Fe/Ni/S catalysts. After purification[31]

* To whom correspondence should be addressed. E-mail: fukutani@
iis.u-tokyo.ac.jp (K.F.), hige@buckyl.kankyo.tohoku.ac.jp (Y.S.).
† The University of Tokyo.
‡ Graduate School of Environmental Studies, Tohoku University.
§ CREST-JST.
ǁ Dowa Holdings Co., Ltd..
⊥ Center for Interdisciplinary Research, Tohoku University.

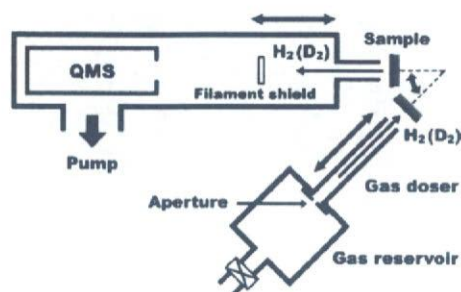14938 *J. Phys. Chem. C, Vol. 111, No. 41, 2007*

Letters

Figure 1. Cryo-TDS apparatus. After gas exposure to the sample with the gas doser, the desorption yield from the sample is measured with the shielded quadrupole mass spectrometer (QMS) as a function of the sample temperature. Both gas doser and shielded QMS are retractable.

of the sample with air oxidation, acid treatment and heating at 1473 K in vacuum (see Supporting Information), remnants of the metal catalysts were lower than 0.45 wt % and the purity of the SWCNTs was higher than 98 wt %, as measured by inductively coupled plasma-optical emission spectrometry (ICP-OES) and thermogravimetry with differential thermal analysis (TG-DTA). The dominant impurities were graphite nanocapsulates and metal encapsulated graphite nanocapsulates. The resultant purified SWCNTs, referred to as "as-purified SWCNTs", are composed of a bundle of 3–30 nm in diameter and ~2.0 μm in length on average, and a SWCNT possesses a diameter of 1.5 nm on average as characterized by Raman scattering spectroscopy and HRTEM. Because heating SWCNTs in O_2 removes the end cap of the tube and causes some additional defects on the tube walls,[32] air-oxidized SWCNTs were prepared by heating the as-purified SWCNTs in a tubular furnace at 723 and 823 K for 30 min under atmospheric conditions (flow rate: 400 mL/min). Adsorption properties of the hydrogen molecules on SWCNTs were characterized with our cryo-TDS apparatus, which consists of retractable gas doser and detector as schematically shown in Figure 1. SWCNTs of ca. 200 μg mixed with ethanol were sprayed onto a polished Cu plate with a size of 10 × 10 mm², and the sample was attached to a liquid-He cooled sample holder. The sample temperature was precisely controlled in the temperature range 10–500 K with a BN heater and a calibrated Si-diode attached on the sample. To avoid residual gas adsorption such as H_2O and CO, the TDS experiments were performed in an ultrahigh vacuum chamber with a base pressure of 2 × 10⁻⁸ Pa. The samples were exposed to either H_2 or D_2 gas with a flux-calibrated gas doser after being cooled to ~10 K. After the dosage, the samples were heated at a ramp rate of 0.25 K/s. During the heating, a quadrupole mass spectrometer (QMS) surrounded by a shield measured desorbing molecules through an aperture of 6 mm in diameter, which faces the sample at a distance of 0.5 mm from the sample. This allows us to detect molecules desorbing exclusively from the sample. The total number of adsorbed H_2 was approximately estimated from the integral TDS intensity by comparing with that of a saturated H layer on Pt(111). No significant intensity at masses other than 2 (4) corresponding to H_2 (D_2) was observed. When the samples were exposed to H_2 (D_2) at 80 K, little hydrogen desorption signal was observed up to 300 K.

Figure 2a is a typical HRTEM image of the as-purified SWCNTs, which shows a bundle of SWCNTs. The tube walls are clearly identified as straight lines, suggesting that this nanotube possesses the well-ordered cylindrical graphene structure. Figure 2b shows a series of TD spectrum of H_2 for the as-purified SWCNTs after various H_2 dosages. At a low dosage of 2 × 10¹⁷/cm², a single peak appears at 20 K with a peak width of 1 K. As the dosage is increased, this peak is
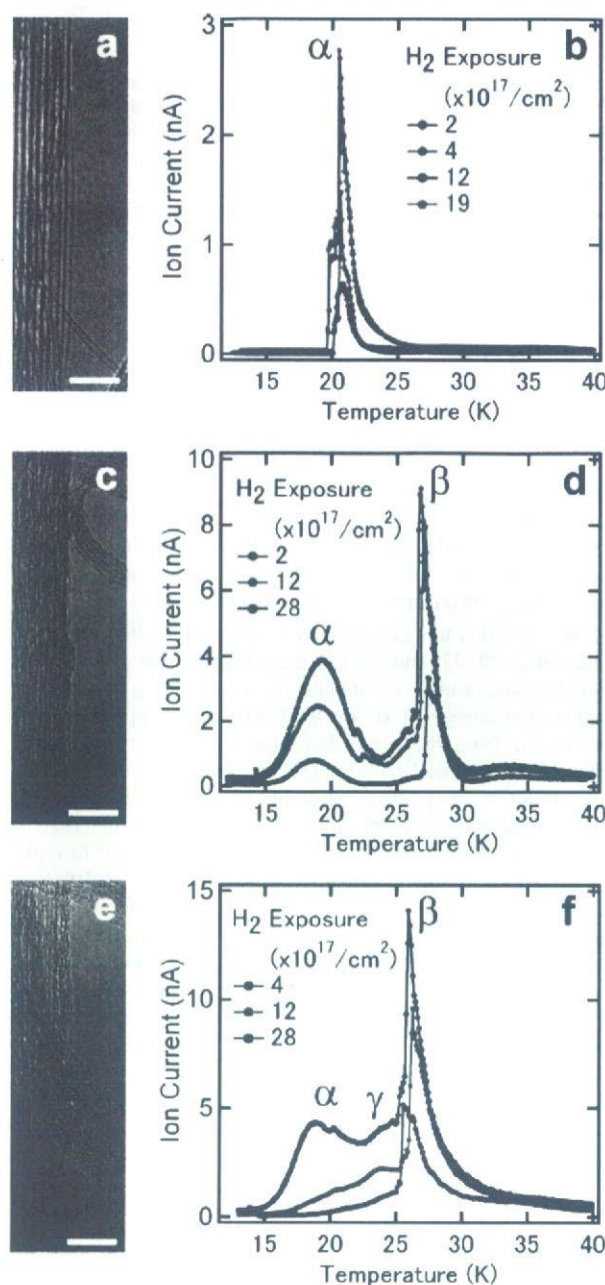

Figure 2. High-resolution transmission electron microscopy images and thermal desorption spectra of H_2 from as-purified SWCNTs (a and b), air-oxidized SWCNTs at 723 K (c and d), and air-oxidized SWCNTs at 823 K (e and f). Scale bar is 10 nm.

increased in intensity, saturating at a dosage of 1 × 10¹⁸/cm² without a shift of the peak temperature. From the integrated intensity of the TDS peak at saturation, the number of H_2 adsorbed on the sample is estimated to be ~10¹⁷/cm². It is noted that there seems to be additional features on the desorption peak as shoulders at higher dosages.

As displayed in the HRTEM images of air-oxidized SWCNTs at 723 K (Figure 2c) and 823 K (Figure 2e), the well-ordered nanotube structure within the bundle disappears and the tube wall looks wavy with its carbon network distorted as a result of air oxidation. This indicates that defects are partially produced at the sidewall and interstitial sidewall of the bundle. The TD spectra of H_2 measured for the air-oxidized SWCNTs at 723 K

Letters

J. Phys. Chem. C, Vol. 111, No. 41, 2007 **14939**

are shown in Figure 2d. In contrast to Figure 2b, the spectra changed dramatically. Whereas the sharp desorption peak observed in Figure 2b gets broadened with a slight shift to a low temperature, another sharp desorption peak appears at 27 K. With increasing H_2 dosage, the intensities of the two peaks increased almost simultaneously, and saturated at a dosage of $\sim 3 \times 10^{18}/cm^2$. Heat treatment of the SWCNTs at a higher temperature brings about a further change in the TD spectrum. Figure 2f shows the TD spectra of H_2 measured for the air-oxidized SWCNTs at 823 K in the atmosphere. In addition to the two components observed in Figure 2d, another broad feature develops at about 24 K filling the gap between the two peaks at 20 and 27 K. The integrated intensities of Figure 2d, f at saturation show that H_2 of $\sim 10^{18}/cm^2$ is adsorbed on the samples. When H_2 and D_2 are sequentially dosed onto these samples, the desorption signals of H_2 and D_2 revealed almost identical spectra as Figures 2b,d,f independent of the order of the H_2 and D_2 dosage. If hydrogen molecules were dissociatively chemisorbed, furthermore, isotope-scrambled HD (hydrogen−deuterium) would be desorbed. Nevertheless, no HD desorption signal was detected, indicating that both H_2 and D_2 were molecularly physisorbed on the SWCNT surfaces.

We note that three characteristic desorption components are present at 20, 27, and ~ 24 K depending on the air-oxidation temperature, which we denote as α, β, and γ peaks. The adsorption energy of H_2 on SWCNTs can be approximately estimated from the peak desorption temperatures with the formula by Redhead[33] assuming that the desorption occurs as a first-order reaction. This assumption is reasonably justified because the hydrogen molecules are in the physisorption regime, not in the dissociative state. Following the Redhead formula, by assuming the preexponential factor to be $2.2 \times 10^{12}/s$ as estimated from the vibrational frequency experimentally measured for hydrogen molecules physisorbed on a Cu surface,[34] we derive the desorption energy for the three components as 50, 65, and ~ 55 meV, respectively. These values seem to be reasonable for the physisorption energy and are well compared with the experimental value of ~ 40 meV reported on a graphite surface[35,36] and theoretically predicted values of 50−100 meV for SWCNTs.[19−24] It should be noted that the α peak in Figure 2b and the β peaks in Figures 2d,f are asymmetric with a sharp rise on the low-temperature side and a tailing feature in the high-temperature side. This seems to contradict the spectrum theoretically expected from the first-order desorption. A possible reason for the sharp rise could be direct and/or indirect intermolecular interaction. As discussed below, H_2 corresponding to the α peak is adsorbed at the groove site (Figure 3a) of the SWCNT bundle, which possibly distorts the bundle structure. Such distortion might stabilize the neighboring molecule leading to effective intermolecular attraction thereby modifying the TDS spectral shape. Because the samples used in the present study are films with thicknesses of ~ 1 μm, on the other hand, the desorption signal might have a delayed component due to diffusion of molecules in the film, which could form a tailing feature in the desorption spectrum.

As confirmed by the HRTEM images and Raman scattering spectra (Figure S2), the three samples are predominantly composed of SWCNT bundles. This implies that the three desorption peaks originate from H_2 physisorbed on the surfaces of SWCNTs. There are four possible adsorption sites of H_2 on the SWCNT bundle as shown in Figure 3a: outside, inside, groove site, and interstitial channel. Recent theoretical work has shown that the physisorption energy of H_2 onto inside and outside walls of a SWCNT is higher and lower than that on a
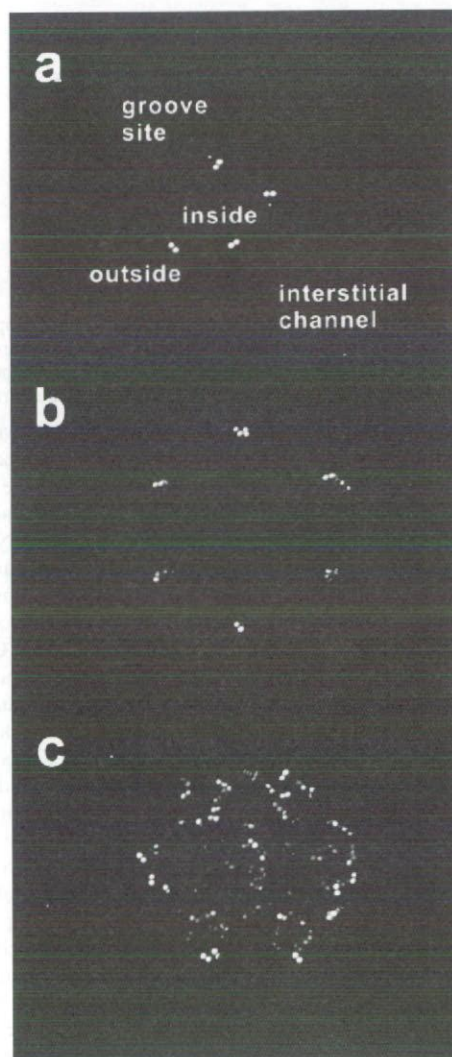

Figure 3. H_2 adsorption on SWCNTs. (a) Cross-sectional view of possible adsorption sites of H_2. (b) Birds-eye view of H_2 adsorbed on a perfect SWCNT bundle. (c) Birds-eye view of H_2 adsorbed on a defective SWCNT bundle.

flat graphene surface, respectively.[19−24] This is because the H_2 molecule inside a tube can see more carbon atoms. Considering the accuracy and reliability of the current first-principles calculation on the van der Waals interaction, only the relative energies between the concave, convex, and flat graphene surfaces should be compared with the experimental data. The physisorption energy of H_2 on a graphite surface is ~ 40 meV according to isotherm studies.[35,36] Our TDS measurement for H_2 on a highly oriented pyrolytic graphite surface reveals a desorption peak at 16 K, which indicates that the physisorption energy is 38 meV in agreement with the literature value. This result, along with the theoretical predictions, suggests that the physisorption energy outside an individual SWCNT is lower than 16 K, which could be outside our measurement range. Without heating in O_2, the SWCNT bundle is expected to be perfect with little defects on the tube wall and with the end cap closed. For this SWCNT sample, the hydrogen molecule can hardly access to the interior of the SWCNT like inside and interstitial channel. According to theoretical calculations, H_2 physisorption energy at the groove site is higher than that on a flat graphene.[23,24] We therefore attribute the sharp α peak
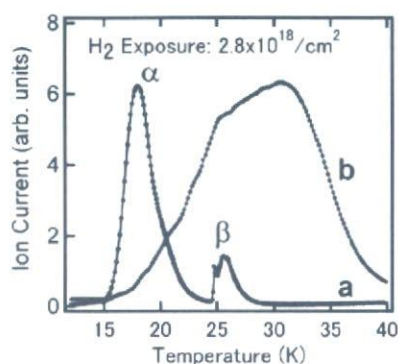
Figure 4. Thermal desorption spectra of H_2 from SWCNTs annealed at 1273 K in Ar for 1 h (a) and air-oxidized SWCNTs at 873 K (b).

observed for the as-purified SWCNTs (Figure 2b) to H_2 adsorbed at the groove site of the SWCNT bundle (Figure 3b).

The desorption peaks observed for the samples with O_2 heating, the β and γ peaks, on the other hand, can be ascribed to the interior of the SWCNT bundle. As schematically shown in Figure 3c, H_2 is considered to be adsorbed at the inside and interstitial channel of SWCNTs. The sharp desorption feature of the α peak in Figure 2b could reflect the intermolecular attraction due to the bundle structure as discussed earlier. As seen in Figures 2d,f, the β peak is also sharp. Because the interstitial channel is structurally similar to the groove site in that both sites consist of multiple SWCNTs, the sharp β peak is possibly attributed to the interstitial channel. This is consistent with the theoretical calculation that the H_2 physisorption energy of the interstitial channel is higher than those of other possible sites.[21,23,24] The γ peak, on the other hand, might be ascribed to H_2 at the inside of SWCNTs. Introduction of defects on the SWCNT walls by O_2 heating should make the groove site inhomogeneous. This could be the reason for the broadening of the α peak due to O_2 heating.[25] As mentioned in the Introduction, the SWCNT structure has been characterized by Raman scattering spectroscopy. In the present work, it was confirmed that the intensity ratio of the D-band representing the defect to the G-band is essentially the same for the as-purified and air-oxidized SWCNTs (Figure S2). Furthermore, TG-DTA exhibits no trace of mass reduction when SWCNTs are treated at 723 K. Nevertheless, the present TDS results clearly indicate that some defects are introduced in the air-oxidized SWCNT samples.

This cryo-TDS was applied to SWCNTs with a different purification procedure. Figure 4a shows a TD spectrum taken for SWCNTs annealed at 1273 K in Ar instead of vacuum as a purification process. Compared with Figure 2b, the spectrum exhibits slight broadening of the α peak and a small intensity of the β peak. Following the above assignment of the two peaks, this sample is considered to contain some defects. When this SWCNT is air-oxidized at 873 K, the TD spectrum was found to change drastically as shown in Figure 4b, where a broad peak appears from 20 to 40 K without any sharp features. This seems to indicate that the bundle structure of SWCNTs is almost lost with tube walls heavily defective. It should be emphasized that the SWCNT sample exclusively showing the α peak with a narrow width (Figure 2b) was obtained only after much effort for growth and delicate purification. We are currently synthesizing SWCNT samples in a more sophisticated way with the aid of HRTEM observation, i.e., individual SWCNT, SWCNTs with only end caps removed and with holes only on the tube walls, and SWCNTs with different diameters and lengths, which we will characterize by H_2 TDS in the near future. This will certainly allow us to correlate the TDS spectral shape including the fine structures with the H_2 adsorption site in more detail and characterize the density and sort of defects of SWCNTs in a sensitive and delicate manner.

Supporting Information Available: Preparation and characterization of samples. This material is available free of charge via the Internet at http://pubs.acs.org.

References and Notes

(1) Saito, R.; Fujita, M.; Dresselhaus, G.; Dresselhaus, M. S. *Phys. Rev. B* **1992**, *46*, 1804–1811.

(2) Hamada, N.; Sawada, S.; Oshiyama, A. *Phys. Rev. Lett.* **1992**, *68*, 1579–1581.

(3) Tanaka, K.; Okahara, K.; Okada, M.; Yamabe, T. *Phys. Chem. Lett.* **1992**, *191*, 469–472.

(4) Zhang, P.; Lammert, P. E.; Crespi, V. H. *Phys. Rev. Lett.* **1998**, *81*, 5346–5349.

(5) Mori, H.; Hirai, Y.; Ogata, S.; Akita, S.; Nakayama, Y. *Jpn. J. Appl. Phys.* **2005**, *44*, L1307–L1309.

(6) Strano, M. S.; Dyke, C. A.; Usrey, M. L.; Barone, P. W.; Allen, M. J.; Shan, H.; Kittrell, C.; Hauge, R. H.; Tour, J. M.; Smalley, R. E. *Science* **2003**, *301*, 1519–1522.

(7) Kong, J.; Franklin, N. R.; Zhou, C.; Chapline, M. G.; Peng, S.; Cho, K.; Dai, H. *Science* **2000**, *287*, 622–625.

(8) Terrones, M.; Ajayan, P. M.; Banhart, F.; Blase, X.; Carroll, D. L.; Charlier, J.-C.; Czerw, R.; Foley, B.; Grobert, N.; Kamalakaran, R.; Kohler-Redlich, P.; Rühle, M.; Seeger, T.; Terrones, H. *Appl. Phys. A* **2002**, *74*, 355–361.

(9) Terrones, M.; Terrones, H.; Banhart, F.; Charlier, J.-C.; Ajayan, P. M. *Science* **2000**, *288*, 1226–1229.

(10) Wei, B.; Spolenak, R.; Kohler-Redlich, P.; Ruhle, M.; Arzt, E. *Appl. Phys. Lett.* **1999**, *74*, 3149–3151.

(11) Kamaras, K.; Itkis, M. E.; Hu, H.; Zhao, B.; Haddon, R. C. *Science* **2003**, *301*, 1501.

(12) Baughman, R. H.; Zakhidov, A. A.; de Heer, W. A. *Science* **2002**, *297*, 787–792.

(13) Kim, U. J.; Furtado, C. A.; Liu, X.; Chen, G.; Eklund, P. C. *J. Am. Chem. Soc.* **2005**, *127*, 15437–15445.

(14) Wang, Y.; Alsmeyer, D. C.; McCreery, R. L. *Chem. Mater.* **1990**, *2*, 557–563.

(15) Hashimoto, A.; Suenaga, K.; Gloter, A.; Urita, K.; Iijima, S. *Nature* **2004**, *430*, 870–873.

(16) Suenaga, K.; Wakabayashi, H.; Koshino, M.; Sato, Y.; Urita, K.; Iijima, S. *Nat. Nanotech.* **2007**, *2*, 358–360.

(17) Fan, Y.; Goldsmith, B. R.; Collins, P. G. *Nat. Mater.* **2005**, *4*, 906–911.

(18) Li, X.; Niu, J.; Zhang, J.; Li, H.; Liu, Z. *J. Phys. Chem. B* **2003**, *107*, 2453–2458.

(19) Okamoto, Y.; Miyamoto, Y. *J. Phys. Chem. B* **2001**, *105*, 3470–3474.

(20) Arellano, J. S.; Molina, L. M.; Rubio, A.; López, M. J.; Alonso, J. A. *J. Chem. Phys.* **2002**, *117*, 2281–2288.

(21) Akai, Y.; Saito, S. *Jpn. J. Appl. Phys.* **2003**, *42*, 640–644.

(22) Ferre-Vilaplana, A. *J. Chem. Phys.* **2005**, *122*, 214724.

(23) Williams, K. A.; Eklund, P. C. *Chem. Phys. Lett.* **2000**, *320*, 352–358.

(24) Zhao, J.; Buldum, A.; Han, J.; Lu, J. P. *Nanotechnology* **2002**, *13*, 195–200.

(25) Xia, Y.; Zhu, J. Z.; Zhao, M.; Li, F.; Huang, B.; Ji, Y.; Liu, X.; Tan, Z.; Song, C.; Yin, Y. *Phys. Rev. B* **2005**, *71*, 075412.

(26) Dillon, A. C.; Jones, K. M.; Bekkedahl, T. A.; Kiang, C. H.; Bethune, D. S.; Heben, M. J. *Nature* **1997**, *386*, 377–379.

(27) Liu, C.; Fan, Y. Y.; Liu, M.; Cong, H. T.; Cheng, H. M.; Dresselhaus, M. S. *Science* **1999**, *286*, 1127–1129.

(28) Dillon, A. C.; Heben, M. J. *Appl. Phys. A* **2001**, *72*, 133–142.

(29) Wilson, T.; Tyburski, A.; DePies, M. R.; Vilches, O. E.; Becquet, D.; Bienfait, M. *J. Low Temp. Phys.* **2002**, *126*, 403−408.

(30) Georgiev, P. A.; Ross, D. K.; De Monte, A.; Montaretto-Marullo, U.; Edwards, R. A. H.; Ramirez-Cuesta, A. J.; Colognesi, D. *J. Phys.: Condens. Matter* **2004**, *16*, L73−L78.

(31) Tohji. K.; Goto, T.; Takahashi, H.; Shinoda, Y.; Shimizu, N.; Jeyadevan, B.; Matsuoka, I.; Saito, Y.; Kasuya, A.; Ohsuna, T.; Hiraga, K.; Nishina, Y. *Nature* **1996**, *383*, 679.

(32) Qingwen, L.; Hao, Y.; Yinchun, Y.; Jin, Z.; Zhongfan, L. *J. Phys. Chem. B* **2002**, *106*, 11085−11088.

(33) Redhead, P. A. *Vacuum* **1962**, *12*, 203−211.

(34) Svensson, K.; Bellman, J.; Hellman, A.; Andersson, S. *Phys. Rev. B* **2005**, *71*, 245402.

(35) Pace, E. L.; Siebert, A. R. *J. Phys. Chem.* **1959**, *63*, 1398−1400.

(36) Vidali, G.; Ihm, G.; Kim, H.-Y.; Cole, M. W. *Surf. Sci. Rep.* **1991**, *12*, 135−181.